LA-UR-15-20029 (Accepted Manuscript)

The global context of the 14 November 2012 storm event

Dixon, P.
MacDonald, E. A.
Funsten, Herbert O.
Glocer, H. O.
Kletzing, C.
Larsen, Brian Arthur
Reeves, Geoffrey D.
Skoug, Ruth M.
Spence, H. E.
Thomsen, M. F.

To be published in: Journal of Geophysical Research: Space Physics

DOI to publisher's version: 10.1002/2014JA020826

Permalink to record: http://permalink.lanl.gov/object/view?what=info:lanl-repo/lareport/LA-UR-15-20029

The global context of the 14 November, 2012 storm event

K.-J. Hwang,[1,2] D. G. Sibeck,[1] M.-C. H. Fok,[1] Y. Zheng,[1] Y. Nishimura,[3] J.-J. Lee,[4] A. Glocer,[1] N. Partamies,[5] H. J. Singer,[6] G. D. Reeves,[7] D. G. Mitchell,[8] C. A. Kletzing,[9] and T. Onsager[6]

K.-J. Hwang, NASA Goddard Laboratory Space Flight Center, Greenbelt, MD 20771, USA. Goddard Planetary Heliophysics Institute, University of Maryland at Baltimore County, Baltimore, MD 21250. (Kyoung-Joo.Hwang@nasa.gov)

D. G. Sibeck, NASA Goddard Laboratory Space Flight Center, Greenbelt, MD 20771, USA. (david.g.sibeck@nasa.gov)

M.-C. H. Fok, NASA Goddard Laboratory Space Flight Center, Greenbelt, MD 20771, USA. (mei-ching.h.fok@nasa.gov)

Y. Zheng, NASA Goddard Laboratory Space Flight Center, Greenbelt, MD 20771, USA. (yihua.zheng@nasa.gov)

Y. Nishimura, Department of Atmospheric and Oceanic Sciences, University of California, Los Angeles, California 90095, USA. (toshi@atmos.ucla.edu)

J.-J. Lee, Solar and Space Weather Research Group, Korea Astronomy and Space Science Institute, Daejeon, South Korea. (jjlee@kasi.re.kr)

A. Glocer, NASA Goddard Laboratory Space Flight Center, Greenbelt, MD 20771, USA. (alex.glocer-1@nasa.gov)

N. Partamies, Finnish Meteorological Institute, Helskinki, Finland. (noora.partamies@fmi.fi)

H. J. Singer, NOAA Space Weather Prediction Center, Boulder, CO 80305, USA. (howard.singer@noaa.gov)

G. D. Reeves, Los Alamos National Laboratory, Los Alamos, NM 87545, USA. (reeves@lanl.gov)

Abstract. From 2 to 5 UT on 14 November, 2012, the Van Allen Probes observed repeated particle flux dropouts during the main phase of a geomagnetic storm as the satellites traversed the post-midnight to dawnside inner magnetosphere. Each flux dropout corresponded to an abrupt change in the magnetic topology, i.e., from a more dipolar configuration to a configuration with magnetic field lines stretched in the dawn-dusk direction. Geosynchronous GOES spacecraft located in the dusk and near-midnight sectors and the LANL constellation with wide local time coverage also observed repeated flux dropouts and stretched field lines with similar occurrence patterns to those of the Van Allen Probe events. THEMIS recorded multiple transient abrupt expansions of the evening-side magnetopause ∼20–30 min prior to the sequential Van Allen Probes observations. Ground-based magnetograms and all sky images demonstrate repeatable features in conjunction with the dropouts. We combine the various in-situ and ground-based measurements to define and understand the global spatiotemporal features associated with the dropouts ob-

D. G. Mitchell, Applied Physics Laboratory, Johns Hopkins University, Laurel, Maryland 20723, USA. (donald.g.mitchell@jhuapl.edu)

C. A. Kletzing, Department of Physics and Astronomy, The University of Iowa, Iowa City, IA 52242, USA. (craig-kletzing@uiowa.edu)

T. Onsager, INOAA Space Weather Prediction Center, Boulder, CO 80305, USA. (terry.onsager@noaa.gov)

[1]NASA Goddard Space Flight Center,

served by the Van Allen Probes. We discuss various proposed hypotheses for the mechanism that plausibly caused this storm-time dropout event as well as formulate a new hypothesis that explains the combined in-situ and ground-based observations: the earthward motion of magnetic flux ropes containing lobe plasmas that form along an extended magnetotail reconnection line in the near-Earth plasma sheet.

Greenbelt, Maryland 20771, USA

1. Introduction

When the interplanetary magnetic field (IMF) turns and remains southward for an extended period of time, substantial disturbances of the Earth's magnetosphere, called geomagnetic storms occur. Major disturbances typically observed during the main phase of geomagnetic storms include strong convection of plasmas from the magnetotail to the inner magnetosphere and resultant ring-current injection which decreases the background magnetic field strength, as quantitatively estimated by the disturbance storm time (Dst) geomagnetic index, i.e., a measure of the averaged deviation of H (north-south) component of the magnetic field near the Earth's equator. The recovery phase, during which the value of the Dst index gradually returns to its pre-storm level, is due to loss of ring-current ions via charge exchange with the neutral exosphere and/or loss to the magnetopause.

In conjunction with geomagnetic storms, energetic electron observations in the radiation belt have shown that the significant decrease in flux during the storm main phase is followed often by a more gradual increase during the recovery phase. Theoretical and observational studies suggest that during the main phase of a geomagnetic storm a build-up of the ring current drives outward radial motion of the electron drift paths to conserve the third adiabatic invariant, i.e., the magnetic flux encircled by a particle's drift orbit. Conservation of the first adiabatic invariant, i.e., the magnetic moment of a gyrating particle subsequently decreases the electron energy flux. This Dst effect, therefore, describes the adiabatic dynamics of trapped radiation belt electrons [*Dessler and Karplus*, 1961;

---

[2]The Goddard Planetary Heliophysics

McIlwain, 1966]. When the fluxes in dropout events often do not return to pre-storm flux levels, there must be real losses via non-adiabatic processes [e.g., *Li et al.*, 1997; *Kim and Chan*, 1997; *Onsager et al.*, 2002; *Green et al.*, 2004].

Loss mechanisms include particle precipitation to the atmosphere and loss to the magnetopause. Atmospheric loss of energetic electrons has been attributed to resonant wave-particle interactions between radiation belt electrons and a variety of plasma waves, such as whistler-mode chorus waves, plasmaspheric hiss, and electromagnetic ion cyclotron (EMIC) waves. Whistler-mode chorus waves are distributed over a broad region from midnight via dawn to noon. Plasmaspheric hiss waves are mostly confined within the dense plasmasphere and within dayside plasmaspheric plumes. EMIC waves are enhanced in the plume and on the dusk-side plasmapause. (See *Thorne* [2010] and references therein.) These waves facilitate pitch angle scattering of electrons into the loss cone, leading to precipitation to the atmosphere [e.g., *Millan and Thorne*, 2007 for a review of loss mechanisms] on time scales of hours (in association with EMIC waves that preferentially resonate with > 0.5 MeV electrons) to day(s) (whistler mode chorus) [*Albert*, 2003; *Meredith et al.*, 2003; *Summers and Thorne*, 2003; *Albert*, 2005; *Horne et al.*, 2005; *Thorne et al.*, 2005]. EMIC waves also resonate with ions, leading to ring current proton precipitation via the scattering of protons into the loss cone [e.g., *Kozyra et al.*, 1997; *Jordanova et al.*, 2001; *Khazanov et al.*, 2002].

More recently, the inward motion of the magnetopause (i.e., compression of the dayside magnetosphere) caused by, for example, the arrival of interplanetary shocks and/or pressure pulses at Earth has been found to result in dropouts of the outer radiation belt

Institute, University of Maryland, Baltimore

65 electrons on open drift paths that were closed before the magnetopause motion [*Des-*
66 *orgher et al.*, 2000]. These magnetopause losses not only affect those electrons that drift

County, Baltimore, Maryland 21250, USA

[3]Department of Atmospheric and Oceanic Sciences, University of California, Los Angeles, California 90095, USA

[4]Solar and Space Weather Research Group, Korea Astronomy and Space Science Institute, Daejeon, South Korea

[5]Finnish Meteorological Institute, Helskinki, Finland

[6]NOAA Space Weather Prediction Center, Boulder, CO 80305, USA.

[7]Los Alamos National Laboratory, Los Alamos, NM 87545, USA.

[8]Applied Physics Laboratory, Johns Hopkins University, Laurel, Maryland 20723, USA

[9]Department of Physics and Astronomy, The University of Iowa, Iowa City, IA 52242, USA.

into the magnetopause but also promote outward radial diffusion via the inward radial gradients created by these losses, producing losses of relativistic electrons, and, as a result, significantly depleting outer belt fluxes on time scales of hours [*Shprits et al.*, 2006]. Numerical and observational studies have shown that the combined effects of outward transport and loss to the magnetopause may act as a dominant loss mechanism, causing energy-dependent dropouts throughout the radiation belt on a time scale of a few hours [*Nishimura et al.*, 2007; *Kim et al.*, 2008; *Ukhorskiy and Sitnov*, 2008; *Loto'aniu et al.*, 2010; *Shprits et al.*, 2012; *Turner et al.*, 2012].

Mechanisms providing replenishment of energetic particles include enhancements of the flux by radial transport or internal energization of trapped drifting electron to > MeV energy level through resonant interaction with waves such as ULF, VLF, and whistler-mode chorus waves by violation of the adiabatic invariants [*Rostoker et al.*, 1998; *Elkington et al.*, 2003; *Meredith et al.*, 2003; *O'Brien et al.*, 2003; *Horne et al.*, 2005; *Loto'aniu et al.*, 2006, 2010; *Reeves et al.*, 2013; *Thorne et al.*, 2013]. Another mechanism is rapid acceleration of lower-energy seed plasma sheet populations injected into the inner magnetosphere as a consequence of magnetic reconnection related to substorm phenomena [*Meredith et al.*, 2001, 2006].

During the main phase of an intense geomagnetic storm (minimum Dst = -108 nT) on 14 November, 2012, abrupt repeated dropouts of both thermal and relativistic populations were observed by NASA's twin spacecraft of the Van Allen Probes, drawing wide attention from the magnetospheric physics community to the need to understand the cause and phenomenological features of the sudden energy-independent dropouts. Various groups sought to model the spatial and temporal observations of the event, reproducing the alter-

nating sequences of nominal and dropout intervals that result from sequential crossings of an open-closed boundary [*MacDonald et al.*, 2013; *Glocer et al.*, 2013]. *Moya et al.* [2014, submitted to J. Geophys. Res.] reported different wave amplitude levels and magnetic field orientations during the quiet and disturbed/dropout intervals, showing the presence of weak kinetic turbulence which dissipates the energy associated with the intermittent discontinuities in the magnetic field during the main phase of the storm.

In this paper, we incorporate in-situ measurements from multi-point spacecraft and ground-based observations to define and understand the global spatiotemporal features associated with the dropouts observed by the Van Allen Probes. Our synthesized analyses allow us to formulate a new hypothesis for the mechanism that caused this abrupt repeated dropout event. The following section presents a brief description of instrumentations we used in this study. In Section 3 we provide an overview of the event detected by the Van Allen Probes, GOES, LANL, and Geotail spacecraft. Using THEMIS measurements of the dayside magnetopause and ground-based observations, we explore the global and temporal features of the magnetic disturbances in association with the particle flux dropouts (Section 4). Section 5 discusses how this event is related to the magnetospheric configuration and dynamics in response to strong external (interplanetary) drivers, and explore various hypotheses proposed for the cause of this storm-time dropout event as well as formulates a new hypothesis, i.e., magnetic flux bundles repeatedly passing those multiple spacecraft, based on the combined in-situ and ground-based observations. Section 6 presents a summary and conclusions.

2. Instrumentation

We used spacecraft and ground-based measurements in this study. In-situ measurements were from the Van Allen Probes (formerly known as the Radiation Belt Storm Probes–RBSP A and B [*Kessel et al.*, 2013; *Mauk et al.*, 2013], terms we will use hereinafter for brevity), the Time History of Events and Macroscale Interactions (THEMIS) spacecraft [*Angelopoulos*, 2008], the geostationary satellite system (GOES) [*Singer et al.*, 1996; *Onsager et al.*, 1996], and the Los Alamos National Laboratory (LANL) instrument [*Reeves et al.*, 1997].

High time-resolution (64 vectors/s) DC magnetic field measurements are obtained from the magnetometer instrument, the Electric and Magnetic Field Instrument Suite and Integrated Science (EMFISIS) [*Kletzing et al.*, 2013] onboard the Van Allen Probes. Plasma data are obtained from the three instruments of the Radiation Belt Storm Probes-Energetic Particle Composition and Thermal Plasma (RBSP-ECT) instrument suite [*Spence et al.*, 2013]: the Helium, Oxygen, Proton, and Electron (HOPE) mass spectrometer [*Funsten et al.*, 2013] measuring electron and ion flux distributions over an entire solid angle on alternating spacecraft spins in the energy range of ∼1 eV–52 keV and distinguishing three ion species, H^+, He^+, and O^+; the Magnetic Electron Ion Spectrometer (MagEIS) [*Blake, J. B. et al.*, 2013] having one low-energy (20–240 keV), two medium-energy (80–1200 keV), and a high-energy (800–4800 keV) spectrometers; the Relativistic Electron and Proton Telescope (REPT) energetic particle instrument [*Baker et al.*, 2012] measuring high-energy electrons of energy range from a few to >10 MeV. Magnetic field measurements aboard THEMIS were made by the Fluxgate Magnetometer (FGM) [*Auster et al.*, 2008] and particle fluxes including onboard plasma moments come

from the Electrostatic Analyzer (ESA) with 3 s time cadence [*McFadden et al.*, 2008]. We also use magnetic field and electron flux measurements from the Magnetometer and the Energetic Particle Sensor (EPS) onboard three GOES-13, 14, and 15 spacecraft [described for earlier satellite series in *Singer et al.*, 1996; *Onsager et al.*, 1996] as well as electron flux measurements from the synchronous orbit particle analyzer (SOPA) instruments on six LANL geosynchronous spacecraft [*Belian et al.*, 1992; *Reeves et al.*, 1997]. Ground measurements were from THEMIS All-Sky Imager (ASI) [*Mende et al.*, 2008], all-sky cameras at the Sodankylä station (SOD) in Finland, and magnetometers at the stations located over the northern America and Europe.

3. Observations of abrupt particle flux dropouts

3.1. The Van Allen Probes observations

From 0100 UT to 0600 UT on 14 November, 2013, during an interval in which the IMF was strongly southward (to be discussed in Section 4.3), the two identical Van Allen Probes observed repeated particle flux dropouts as they passed through the post-midnight to dawnside inner magnetosphere [see Figure 1 showing spacecraft locations in Geocentric Solar Magnetospheric (GSM) coordinates each hour from 0100 UT (large triangle) to 0600 UT]. Figure 2 shows the Van Allen Probes observations between 0100 and 0630 UT. Panels (a-c) present the (x, y, z) components of the magnetic field for RBSP-A (blue) and RBSP-B (red) and (d, e) the electron flux spectrogram measured by the ECT/MagEIS instrument aboard RBSP-A and RBSP-B, respectively.

Both RBSP-A and B observed repeated abrupt dropouts in particle flux (Figure 2d and e), as bounded by pairs of dot-dashed vertical lines. The dropouts are seen for ions of all species (Figure 3b-d) and for both thermal and energetic electrons (Figure 2d and Figure

3e, f) measured by ECT/HOPE, ECT/MagEIS, ECT/REPT, and RBSPICE. Note that the enhanced fluxes of low-energy ions (below a few hundred eV in 3b and c) observed by HOPE are due to the effects of spacecraft potential, which is often elevated during storm times and accelerates these low-energy particles into the detector. The fact that the sudden reductions in particle flux immediately recover during undisturbed periods following the sequential dropouts is an indication of transient or local phenomena, unlike the long-term storm-associated loss of particles mentioned in Section 1.

There are intense magnetic-field variations during the disturbed (dropout) times (Figure 2a-c): B_x and B_z decrease in magnitude while B_y increases along the $-y$ direction, characterizing events by large magnetic strength. Note that (1) prior to the event, e.g., during ∼0130-∼0155 UT, the magnetic field measurements ($\sqrt{B_x^2 + B_y^2} > |B_z|$) indicate an unusually highly stretched status of the inner magnetosphere, (2) each dropout is often preceded by a small dip in B_x (arrows in Figure 2a) and ends with a sharp transient B_z increase (arrows in Figure 2c) except the first dropout occurring at ∼0200 UT where B_z profiles are bipolar rather than transiently peaked over an extended period of the dropout signature starting from ∼0155 UT (marked by another dot-dashed vertical line associated with the first dropout), indicated by a precursive reduction in the electron flux (Figure 2d), to ∼0205 UT.

RBSP-B follows the trajectory of RBSP-A (Figure 1), missing the first dropout, yet observing a final dropout at ∼0507 UT that was not detected by RBSP-A. RBSP-B also observed a weak flux depression from 0543:15 UT to 0551:30 UT, during which the magnetic field varies in similar patterns to those for intense dropouts. Having each

encountered five abrupt dropouts (marked by red shading at the bottom of Figure 2), the two Van Allen Probes subsequently headed towards perigee.

3.2. The GEO observations

GOES-13, 14, 15 traced geosynchronous orbits (GEO) through the dusk and near-midnight sectors from 0100 to 0600 UT (Figure 1). Figure 4 shows the magnetic field and electron and proton particle fluxes measured by the three probes. Simultaneous changes in the magnetic field and particle flux are seen more clearly towards dusk and farther from the near-midnight sector. In particular, the number of those intermittent changes and their periodicity observed by GOES-15 (bottom three panels in Figure 4), residing mostly in the dusk sector during the event, shows some similarity to the Van Allen Probes observations. Noteworthy differences between the GOES-15 and the Van Allen Probes measurements are (1) although similar features associated with flux dropouts are detected both in the dawn (Van Allen Probes) and the dusk (GOES-15) sectors, there is no one-to-one correspondence and they are not often coincident, i.e., GOES-15 observes the second to fifth dropouts $9 - 15$ min earlier than those at the Van Allen Probes (see Table 1) ; (2) electron and proton particle flux dropouts sometimes do not correspond (indicated by vertical magenta lines), and decreases are often bounded by flux increases (see dot-dashed vertical lines in Figure 4); (3) patterns of the magnetic-field disturbances during the dropout intervals also vary, but the most common are enhancements along the anti-earthward and northward directions. GOES-15 also often displays a gradual change in the magnetic field prior to the time of maximized dropouts unlike the sudden changes in magnetic morphology observed by the Van Allen Probes. The gradual change before the event peaks, which is followed by a fast recovery (for example, see the magetic field

variations around the dropout occurring at ∼0255 UT) possibly indicates a developmental phase before the onset of the dynamics causing flux dropouts or a precursor to remotely approaching structures associated with dropouts.

Additional GEO observations providing further local time coverage are obtained from the LANL constellation (see Figure 1). Figure 5 shows that the six LANL spacecraft also encountered intermittent electron flux dropouts and simultaneous reductions in proton flux (not shown). Three noticeable dropouts are detected by LANL-97A, LANL-04A, and LANL-02A, sequentially (red arrows in Figure 5), indicating azimuthal propagation. LANL-01A and 1991-080, situated in the afternoon sector and slightly behind the dusk terminator during 0150–0420 UT and 0300–0530 UT, respectively, experienced prolonged periods of flux reduction. Interestingly, although 1991-080 was located close to GOES-15, the two spacecraft measured remarkably different particle flux variations. We find that the magnetic latitudes of LANL-01A and 1991-080 obtained from the T96 model [*Tsyganenko*, 1995] range between -10° and -30° during the extended dropout intervals [*MacDonald et al.*, 2013], compared to that of GOES-15, which falls within 10° of the magnetic equator. These latitudinal differences between GOES and LANL observations will be discussed further when constructing the global features of these events in Section 4.

3.3. The Geotail observations

Geotail traversed the outer dawn-side magnetosphere toward the morning magnetopause during the period of interest (Figure 1). Figure 6 shows (a) the magnetic field, (b) energetic electron flux, (c, d) energetic ion flux, (e, f) thermal ion and electron flux. [There was no data available between 0430 UT and 0630 UT.] Geotail made a short excursion to the

magnetosheath from ∼0315 to ∼0345 UT, as indicated by a southward B_z component (Figure 6a), a cold dense low-energy (a few hundreds eV or below) populations, and the sharp decrease in energetic ion populations (Figure 6e, f). Interestingly, Geotail also observed repeated losses of both thermal and energetic particle flux bounded by pairs of dot-dashed vertical lines at ∼0202, 0300, and 0415 UT. Although less clear than in the case of the Van Allen Probes observations, the magnetic strength also increases during these reduced flux intervals, each of which is marked by an enhancement in the dawnward ($-B_y$) component of the magnetic field.

4. Propagation of signatures associated with flux dropouts

4.1. Timing analyses of flux-dropout structures

Although the flux dropouts/reductions and corresponding magnetic topology changes occur intermittently with comparable periodicity at many magnetospheric locations, their occurrence patterns generally show no clear one-to-one correspondences. We combined all in-situ measurements available for the event, presented in Section 2, to see if any propagation signatures are revealed. Table 1 lists the observation times for each spacecraft detection of the onset time (upper number) and the peak flux depression time (lower number) of the series of flux reduction. Times of weak flux reductions are in parentheses. A thick vertical line separates post-midnight/dawn-side observation times from pre-midnight/dusk-side ones.

The first dropout around at 0200 UT is observed, in sequence, by LANL-97A, RBSP-A, Geotail, LANL-04A, and LANL-02A, i.e., from post-midnight to dawn and towards morning sector as indicated by spacecraft locations in Figure 1. Later dropouts are, in general, consistent with this trend, as was shown from three LANL (LANL-97A, LANL-04A, and

LANL-02A) observations in Section 3.2. However, the third dropout was measured by LANL-97A at ∼0336 UT, about 0.5 (2.0) min later than RBSP-A (B). During the third event, LANL-97A was located azimuthally closer to midnight but radially outward from the two probes, suggesting that this dropout signature propagated slightly outward in the radial direction in the dawn sector together with its azimuthal motion. [The underlying assumptions are that the dropout sigantures propagate like a planar discontinuity and propagation normals approximately lie on the equatorial plane.] Figure 2, in fact, demonstrates that RBSP-B, located azimuthally closer to midnight in local time and/or more earthward than RBSP-A during the first to third dropout times, detected each event ∼1–5 minutes earlier than RBSP-A.

Pre-midnight/dusk observations from GOES-13, 14, and 15, LANL 1991-080 and 1994-084 provide less evidence for propagating features. However, the fourth dropout at ∼0400 UT, observed sequentially by 1994-084, GOES-13, 14, and 15 (and/or 1991-080 observing an extended event until 0422 UT) also suggests azimuthal propagation away from midnight.

These timing analyses in general indicate that the dropout-associated signatures propagate azimuthally away from midnight. Observations by spacecraft beyond geosynchronous orbit in the dawn sector also suggest that they propagate slightly radially outward. This propagation signature is consistent with ground magnetometer data near the stations magnetically conjugate to the Van Allen Probes that show clear evidence for the eastward propagation of repeated disturbances (negative bays in H-component and often positive peaks in D-component, not shown). Ground magnetograms in the dusk sector show

complicated disturbances. Nonetheless, consecutive disturbances characterized mainly by negative bays in H- and D-components are suggested to propagate westward (not shown).

4.2. All sky images

The overall propagation pattern of the dropout-associated features suggests event origin in the magnetotail, followed by their earthward propagation to the inner magnetosphere, and subsequent divergence to both dawn and dusk. We use all sky images, which provide an effective 2-D display of the physical processes occurring in the magnetotail, to explore this possibility. The THEMIS All-Sky Imager (ASI) [*Mende et al.*, 2008] data shown in Figure 7A demonstrate that narrow north-south auroral forms, called auroral streamers (marked by red arrows), appeared prior to each dropout. The streamers were primarily seen at the stations, KUUJ (58.10° north and 291.60° east in geographic latitute and longitude), SNKQ (56.54° N and 280.77° E), and GILL (56.35° N and 295.34° E). They mapped to the pre-midnight magnetotail during the event and propagated predominantly towards lower latitudes, corresponding to earthward motion in the magnetotail. They soon developed into, or coincided with, striated auroral structures that were extended in the east-west direction.

The auroral keogram recorded at the subauroral Sodankylä station (SOD, 67.42° N and 26.39° E) in Finland close to the magnetic footprints of the Van Allen Probes according to T96 model [*Tsyganenko*, 1995] shows that some disappearances of auroral intensifications correspond to the Van Allen Probes flux dropouts (indicated by vertical solid magenta lines Figure 7B). Note that we plotted the image assuming that the height of the emission is at 110 km. [*Sangalli et al.*, 2011]. The resulting forms of auroral intensity surrounding the disappearance region suggest undulations of the poleward boundary

of auroral emission. Some of those features are omega bands, which are diffuse aurora distorted to an omega shape. The disappearances propagated to lower latitudes (blue arrows), again mapping earthward motion in the magnetotail, and eastward or azimuthally away from midnight (as consecutively observed at increasing magnetic longitudes). Time lags between (geographic) longitudes and durations of disappearance features seen in the keogram provide estimates for the azimuthal speed and size of the region: The azimuthal size of the disappearance region is ∼200–430 km, and its eastward speed is ∼0.8–1.2 km/s in the ionosphere. These numbers map to ∼0.5–1.1 R_E and 14–20 km/s in the magnetosphere according to the T96 model. The derived azimuthal velocity is consistent with the ∼2–5 min lag for (averaged) event motion between RBSP-B and RBSP-A.

4.3. THEMIS observations of the magnetopause and upstream solar wind conditions

As indicated in Figure 1, the two ARTEMIS spacecraft (THEMIS-B and C), lying upstream from Earth and near the Sun-Earth line ($x \approx 57$ R_E) during the event, provide solar wind observations. Three THEMIS spacecraft (THEMIS-A, D, and E) monitored the response of the dayside magnetopause in the post-noon sector. Figure 8 shows (a) the IMF and (b) the solar wind (dynamic, thermal, magnetic, and total) pressures and density observed by THEMIS-C. Panels (c) and (g) depict the magnetic field, (d, h) the bulk plasma flow velocity, (e, i) the plasma temperature and density, and (f, j) the ion energy spectrogram measured by THEMIS-A (middle panels) and D (bottom panels).

During the event, THEMIS-C observed an IMF that pointed strongly southward with a y-component that changed from duskward ($+B_y$) to dawnward ($-B_y$). THEMIS-E and THEMIS-A, which were on an outbound trajectory behind THEMIS-D, spent most

of the interval from 0100 UT to 0630 UT in the magnetosheath, as indicated by the southward magnetic field, $-B_z$, significant flow velocities in the anti-sunward ($-V_x$) and duskward ($+V_y$) directions, low ($\lesssim$ 200 eV) temperatures with high densities, and larger ion populations below ~1 keV. THEMIS-A and THEMIS-D did make multiple intermittent excursions into the magnetosphere and/or its magnetopause current layer, where ~10 keV magnetospheric ions leaking out from the magnetosphere coexist with magnetosheath plasmas (Figure 8j), at times marked by red vertical dot-dashed lines. The magnetosphere can be characterized by $+B_z$, reduced flow velocities, higher temperatures with lower densities, and ion populations with energies above ~1 keV. The multiple magnetopause or boundary-layer crossings indicate that the dayside magnetosphere repeatedly expanded outward and contracted. About 13–15 min before each of these dayside expansion episodes, THEMIS-C consistently observed reduced solar wind (dynamic) pressures, primarily resulting from depressed densities (blue shading in Figure 8). The ~13–15-min interval corresponds well to the time required for solar-wind features transit from THEMIS-C to THEMIS-A/D with an average velocity of $V_x \approx -380$ km/s as observed by THEMIS-C (not shown), suggesting that the repeated dayside expansions were triggered by intermittent reductions in the solar wind dynamic pressure.

The number of times that the dayside magnetopause was abruptly disturbed (expanded) is similar to the number of flux dropouts observed by the Van Allen Probes (denoted by red shaded regions at the bottom of Figure 8). The first expansion occurred ~5 min prior to the first dropout at the Van Allen Probes. Later magnetopause expansions precede each of the following dropouts by ~20–30 min, except for the fifth dropout (marked by light red shading at the bottom of Figure 8) that follows ~5 min after the dayside

expansion. Furthermore, the longest dayside expansion beginning at ∼0303 UT can be linked to the longest duration dropout feature starting at ∼0333 UT at the Van Allen probes. In Section 5, we review previously proposed hypotheses about the dynamics causing the flux dropouts and formulate a new one that can plausibly explain multi-spacecraft measurements of dropout-associated signatures including our timing analysis results.

5. Magnetospheric dynamics causing the flux dropouts

A number of researchers have addressed the multiple abrupt flux dropouts that are observed by the Van Allen Probes deep ($L \approx 5$) within the magnetosphere. Some attribute these dropouts to duskward then dawnward IMF and the strongly southward IMF during the storm (Figure 8a). The IMF-B_y component might have caused a substantial tilt of the magnetotail current sheet (or magnetic equatorial plane), placing the Van Allen Probes repeatedly in the open field-line (lobe-like) region where rarefied plasmas of both thermal and energetic populations are present [*Cowley*, 1981; *Khurana et al.*, 1996]. Because the Earths dipole lies relatively close on the noon-midnight meridional plane during the event, the effects of the dipole tilt on the dawn-dusk tilt of the magnetotail current sheet are insignificant.

However, the predicted IMF-B_y tilt effect and the magnetic field variations observed by the Van Allen Probes during the dropout events are inconsistent: The first three dropouts from ∼0200 UT to 0340 UT occurred during a positive IMF-B_y (Figure 8), under which the magnetotail plasma and current sheets should tilt counter-clockwise when seen from the Sun, since dayside reconnection adds flux to the northern dawn and southern dusk lobes under these conditions. The nearly equatorial Van Allen Probes should then lie

north of the equator and observe a positive B_y. However, as illustrated in Figure 2(b), the Van Allen Probes observe a strongly negative B_y when they enter the flux dropout regions. Furthermore, as seen in Figure 8(a), IMF-B_y changes sign from positive to negative at ∼0330 UT during the period of the event. The sense of tail plasma sheet tilt should, accordingly, change from counter-clockwise to clockwise when the flux resulting from dayside reconnection is deposited in the northern dusk and southern dawn lobes. The equatorial Van Allen Probes should then lie south of the tilted equator and observe a negative B_y. However, as seen in Figure 2(b), the probes observe a weaker negative B_y during the fourth to sixth dropouts (after ∼0345 UT) than they did during earlier dropouts.

The extended period of strong IMF intensity might have caused unusually stretched magnetotail configurations and/or north/south compressions of the magnetosphere, as indicated by the stretched magnetic field lines ($\sqrt{B_x^2 + B_y^2} > |B_z|$) in the inner magnetosphere at the Van Allen Probes location (Figure 2a-c). From the negative B_y that the probes observed, we know that the Van Allen Probes were located south of the magnetic equator. The large IMF might distort magnetospheric magnetic fields and cause these spacecraft to lie near the boundary between the plasma sheet and the southern lobe, occasionally crossing the open-closed boundary according to the magnetospheric responses to the solar wind driver. *Glocer et al.* [2013] and *MacDonald et al.* [2013] developed this scenario and successfully reproduced the Van Allen Probes and LANL observations using the global MHD numerical codes and field-line mapping technique. The different times when the various spacecraft observe the series of flux decrease in the dawn and the dusk sector would result from local structure in the open-closed boundary.

Another interpretation of the Van Allen Probes flux dropout is that a series of plasma bubbles are created in the magnetotail and propagate earthward past the RBSP-B and A spacecraft, consecutively [*Lee et al.*, 2013]. The IMF-B_y-associated tilting and/or global compression/stretching of the magnetosphere should be more readily detected at the flanks of the magnetosphere than near midnight, which is opposite to the Van Allen Probes and LANL observations (Section 3.1 and 3.2). The bubble scenario, therefore, interprets each event as a localized, transient phenomenon, requiring no clear one-to-one correspondence of the dropout observations amongst widely-distributed spacecraft. However, we note that plasma bubbles that are characterized by low entropy are expected to penetrate radially inward via the interchange instability, which is not consistent with our multi-spacecraft timing analyses of the mainly azimuthal, but also radially outward propagation of the dropout signatures (see Figure 9A). More importantly, the rapid and intense magnetic signatures during the dropouts cannot be explained by this hypothesis because a localized bubble that carries a large negative B_y within it cannot penetrate into the dipolar inner magnetosphere.

We, therefore, formulate a new hypothesis where the flux-depleted regions are interpreted as magnetic flux bundles or flux ropes (Figure 9). These events occurred during the extended period of strong southward IMF, which caused magnetotail reconnection to proceed from closed plasma sheet to open lobe magnetic fields, with time. The strong IMF also leads the plasma sheet to thin enough that the tearing instability occurs at multiple places along the tail current sheet, generating flux ropes that contain low-density lobe plasmas as a result of the extended lobe reconnection and a significant axial (y -directional) magnetic field component associated with a guide field of reconnection. Supposing that

intermittent decreases in the solar wind dynamic pressure or other unknown driver inherent in the solar wind lead the dayside magnetopause to expand outward, the flux added to the northern/southern lobes and tail due to dayside reconnection will most largely compress the magnetotail region tailward of the previously thinned location, causing the site of magnetotail reconnection to move anti-sunward. Then, the outflow jets earthward of the new (and more distant tail) reconnection site push the previously-formed flux ropes earthward. When these ropes reach the region of strong pressure gradients in the inner magnetosphere, they cannot penetrate further, and then start to wrap around the boundary, possibly moving to the northern or southern hemisphere off the equator.

The flux-rope scenario explains a majority of the observational features: (1) The lack of precise timing coincidence between the dawn and dusk observations can be explained by the fact that the flux-rope motion drifting in the dawn and the dusk sector will depend on the local environments. The bursty bulk flow events [*Angelopoulos et al.*, 1992] observed more often and/or stronger in pre-midnight sector than post-midnight [*Angelopoulos et al.*, 1994; *Dubyagin et al.*, 2010] may also explain the GOES observations of dusk-side dropouts that are $9-15$ min earlier than the dawn-side Van Allen Probes observations. (2) The time lags of $\sim$20–30 min from the THEMIS to the Van Allen Probes observations can correspond to the duration required for the dayside dynamics to lead the nightside responses. (3) The particle flux enhancement bounding the flux rope (flux dropouts) might be caused by intense magnetic field squeezing particles out of the flux rope into the surrounding region [*Shirataka et al.*, 2006] and/or compression of the flux ropes on either side of the flux rope, thereby explaining the GOES observations of the flux-depleted regions surrounded by short-range flux increases (Figure 4). (4) The equatorward auroral streamers

seen before each dropout event and the striated, horizontally elongated structures, which develop shortly after those streamers, also support this scenario, corresponding to the earthward propagation of flux ropes and their draping around the pressure gradients, respectively. (5) The draping and/or spreading of flux ropes in the azimuthal direction (θ) disturb background magnetic fields, generating field-aligned currents ($J_{||(z)} \approx -\frac{1}{r}\frac{\partial B_r}{\partial \theta}$), which explain the magnetogram variations in the dawn and dusk sectors (the reversals in D-components); Such disturbances in the magnetic field coupled to the auroral region can generate undulations of the poleward boundary of auroral emission or omega bands (Section 4.2).

Figure 10A lists boundary normals during the inbound and outbound crossings of each dropout region by the Van Allen Probes, calculated via magnetic-field minimum variance analysis [*Paschmann et al.*, 1998]. These normal directions observed by RBSP-A (left) and RBSP-B (right) are visualized in 3D in Figure 10B. Most normals for entrances into the flux dropout region point in the z direction whereas most normals for exits point in the x direction. Figure 11A illustrates the trajectory of the Van Allen Probes with respect to a motional magnetic flux rope. Since the spacecraft were nearly stationary, it must be the flux rope that moves past them. This cartoon explains the small dip (increase in magnitude) in the B_x components and sharp increases in B_z components at the entrance and exit of each dropout, respectively, that were noted in Section 2.1 and Figure 2.

Figure 11B demonstrates that the magnetic field variations observed during a single flux-dropout structure can be relatively well fit to a force-free flux rope model, where $\mu_0\mathbf{J} = \alpha\mathbf{B}$ (so that $\mathbf{J} \times \mathbf{B} = 0$). For a constant α, Ampere's law becomes a Helmholtz equation whose solutions are Bessel functions [*Lundquist*, 1950]. The flux rope in a force-free configuration

has a cylindrical symmetry, represented by the axial (B_A), tangential (B_T), and radial (B_R) components of the magnetic field: $B_A = B_0 J_0(aR)$, $B_T = B_0 H J_1(aR)$, and $B_R = 0$, where R is the distance from the axis, $H = \pm 1$ determines the handedness of the magnetic field, and B_0 and a are constants determined by the fit. Figure 11B shows the axial (b) and tangential (c) components, and the angle (d) made by the axial component to the total magnetic strength (with 90° corresponding to the core of the flux rope) during the fourth dropout episode at ∼0417–0429 UT (dot-dashed curves in Figure 11B). Overplotted are the model values shown in solid curves. H is found to be -1. B_0 and a in our fit are -182.0 nT and 7.9 R_E^{-1} with a standard deviation of 0.10 and 0.14. These numbers correspond to an estimated magnetic flux of $\sim 1.4 \times 10^6$ Wb within a flux rope with a diameter of ∼0.61 R_E (∼3900 km), which is consistent with the size of the auroral-emission disappearance regions (or omega bands) in Section 4.2. Fitting for other flux-dropout structures yields standard deviations of fitted B_0 and a ranging ≤ 0.25 and ≤ 0.17, respectively, indicating a reasonable consistency between the measurements and the model-predictions.

6. Conclusions

This paper presents multi-spacecraft observations of the storm-time inner and outer magnetosphere during a multiple flux-dropout event, initially identified by the Van Allen Probes that exhibited considerable abruptness and intermittency. The event can be further distinguished from the flux dropouts typically observed during the main phase of geomagnetic storms by the unusual magnetic field topology (strong B_y) simultaneously observed with the dropout occurrence. We combined various measurements from in-situ spacecraft and ground-based magnetosphere monitors to define and understand the global features associated with the dropouts. The GOES, LANL, and Geotail spacecraft simi-

larly detected sudden repeated loss of particle flux and/or corresponding magnetic-field changes with a similar occurrence frequency to the Van Allen Probes measurements. However, observational discrepancies in occurrence times and flux variation patterns between those spacecraft differing in locations demonstrate that local magnetic geometry and/or plasma environments determine the encounter of the event whatever generation mechanisms underlying the event are. We reviewed hypotheses for the cause of the flux dropouts, including crossings of the open-closed boundary and plasma bubble scenarios. We also formulated a new hypothesis, i.e., a magnetic flux rope scenario, after combining dayside magnetopause observations and multiple inner/outer magnetosphere data, together with ground-based measurements (all sky images, keogram, and magnetograms). This hypothesis explains various features of the Van Allen Probes (and GEO) observations including time lags between the satellites detecting dropouts, repeated magnetic variations (B_x dips and B_z peaks) with inbound/outbound normals when the probes entering/exiting the flux dropout region, the size of the flux ropes predicted by a model fit, and short-range flux increases surrounding the flux-depleted regions.

The sequence of events suggests strongly that the magnetospheric process triggering or facilitating the event may have originated in the tail current sheet, then caused dropout-associated signatures to propagate earthward and azimuthally away from the midnight. The present event occurred when the magnetosphere was unusually highly stretched or compressed in the north-south direction retains plenty of room for further studies in the aspect of magnetospheric responses to strong interplanetary drivers. The global spatiotemporal context of the event we constructed using multi-spacecraft and ground-based measurements helps understand such a unique case study.

Acknowledgments. This study was supported, in part, by NASA's Van Allen Probes grant to the Goddard Space Flight Center with data from THEMIS, GOES, LANL, Geotail missiions, ground magnetometers, and all sky imagers. Geotail, Van Allen Probes, and THEMIS datasets were provided by the Space Physics Data Facility at Goddard Space Flight Center through their Coordinated Data Analysis Web (http://cdaweb.gsfc.nasa.gov) and THEMIS Web (http://themis.ssl.berkeley.edu/). We acknowledge S. Claudepierre for providing data from the MagEIS instrument of the Van Allen Probes Mission. H. Singer (howard.singer@noaa.gov), G. Reeves (reeves@lanl.gov), N. Partamies (noora.partamies@fmi.fi), and Y. Nishimura (toshi@atmos.ucla.edu) provided GOES, LANL, auroral keogram, and high-resolution all sky image data, respectively. KJH thanks E. A. MacDonald for useful discussions. A portion of this work was supported by NSF Magnetospheric Physics grant No. AGS-1305374.

References

Albert, J. M. (2003), Evaluation of quasi-linear diffusion coefficients for EMIC waves in a multispecies plasma, *J. Geophys. Res.*, *108(A06)*, 1249, doi:10.1029/2002JA009792.

Albert, J. M. (2005), Evaluation of quasi-linear diffusion coefficients for whistler mode waves in a plasma with arbitrary density ratio, *J. Geophys. Res.*, *110*, A03218, doi:10.1029/2004JA010844.

Angelopoulos, V. (2008), The THEMIS Mission, *Space Sci. Rev.*, *141*, 5.

Angelopoulos, V., W. Baumjohann, C. F. Kennel, F. V. Coroniti, M. G. Kivelson, R. Pellat, R. J. Walker, H. Lühr, and G. Paschmann (1992), Bursty bulk flows in the inner central plasma sheet, *J. Geophys. Res.*, *97*, 4027–4039.

Angelopoulos, V., C. F. Kennel, F. V. Coroniti, R. Pellat, M. G. Kivelson, R. J. Walker, W. Baumjohann, W. C. Feldman, and J. T. Gosling (1994), Statistical characteristics of bursty bulk flow events, *J. Geophys. Res.*, *99*, 21,257–21,280.

Auster, H. U., et al. (2008), The THEMIS fluxgate magnetometer, *Space Sci. Rev.*, *141*, 235–264, doi:10.1007/s11214-008-9365-9.

Baker, D. N., et al. (2012), The relativistic electron-proton telescope (REPT) instrument on board the radiation belt storm probes (RBSP) spacecraft: Characterization of Earth's radiation belt high-energy particle populations, *Space Sci. Rev.*, *179*, 337–381, doi:10.1007/s11214-012-9950-9.

Belian, R. D., G. R. Gisler, T. Cayton, and R. Christensen (1992), High Z energetic particles at geosynchronous orbit during the great solar proton event of October 1989, *J. Geophys. Res.*, *97(A11)*, 16,897–16,906, doi:10.1029/92JA01139.

Blake, J. B. et al. (2013), The magnetic electron ion spectrometer (MagEIS) instruments aboard the radiation belt storm probes (RBSP) spacecraft, *Space Sci. Rev.*, *179*, 383, doi:10.1007/s11214-013-9991-8.

Cowley, S. W. H. (1981), Magnetospheric asymmetries associated with the y-component of the IMF, *Planet. Space Sci.*, *29*, 79, doi:10.1016/0032-0633(81)90141-0.

Desorgher, L., P. Buhler, A. Zehnder, and E. O. Fluckiger (2000), Simulation of the outer radiation belt electron flux decrease during March 26, 1995, magnetic storm, *J. Geophys. Res.*, *105*, 21,211, doi:10.1029/2000JA900060.

Dessler, A. J., and R. Karplus (1961), Some effects of diamagnetic ring currents on van allen radiation, *J. Geophys. Res.*, *66*, 2289, doi:10.1029/JZ066i008p02289.

Dubyagin, S., V. Sergeev, S. Apatenkov, V. Angelopoulos, R. Nakamura, J. McFadden, D. Larson, and J. Bonnell (2010), Pressure and entropy changes in the flow-braking region during magnetic field dipolarization, *J. Geophys. Res.*, *115*, A10225, doi:10.1029/2010JA015625.

Elkington, S., M. M. K. Hudson, and A. A. Chan (2003), Resonant acceleration and diffusion of outer zone electrons in an asymmetric geomagnetic field, *J. Geophys. Res.*, *108*, A3111, doi:10.1029/2001JA009202.

Funsten, H. O., et al. (2013), Helium, Oxygen, Proton, and Electron (HOPE) mass spectrometer for the Radiation Belt Storm Probes Mission, *Space Sci. Rev.*, *179*, 423–484, doi:10.1007/s11214-013-9968-7.

Glocer, A., N. Buzulukova, M. H. Fok, D. G. Sibeck, and S. Chen (2013), Multi-physics simulations of Van Allen Probes observations of November 14th 2012, *Eos Trans. AGU*, pp. SM33C–05.

544 Green, J. C., T. G. Onsager, T. P. O'Brien, and D. N. Baker (2004), Testing loss mecha-
545 nisms capable of rapidly depleting relativistic electron flux in the Earth's outer radiation
546 belt, *J. Geophys. Res.*, *109*, A12211, doi:10.1029/2004JA010579.
547 Horne, R., R. M. Thorne, S. A. Glauert, J. M. Albert, N. P. Meredith, and R. R. Ander-
548 son (2005), Timescale for radiation belt electron acceleration by whistler-model chorus
549 waves, *J. Geophys. Res.*, *110*, A03225, doi:10.1029/2004JA010811.
550 Jordanova, V. K., C. J. Farrugia, R. M. Thorne, G. V. Khazanov, G. D. Reeves, and
551 M. F. Thomsen (2001), Modeling ring current proton precipitation by electromagnetic
552 ion cyclotron waves during the May 14-16, 1997, storm, *J. Geophys. Res.*, *106*, 7–22,
553 doi:10.1029/2000JA002008.
554 Kawano, H., and T. Higuchi (1995), The bootstrap method in space physics: error esti-
555 mation for the minimum-variance analysis, *Geophys. Res. Lett.*, *22*, 307.
556 Kessel, R. L., N. J. Fox, and N. Weiss (2013), The Radiation Belt Storm Probes (RBSP)
557 and Space Weather, *Space Sci. Rev.*, *179*, 531–543, doi:10.1007/s11214-012-9953-6.
558 Khazanov, G. V., K. V. Gamayunov, V. K. Jordanova, and E. N. Krivorutsky (2002),
559 A self-consistent model of the interacting ring current ions and electromagnetic ion cy-
560 clotron waves, initial results: Waves and precipitation fluxes, *J. Geophys. Res.*, *107(A6)*,
561 7–22, doi:10.1029/2001JA000180.
562 Khurana, K. K., R. J. Walker, and T. Ogino (1996), Magnetospheric convection in the
563 presence of interplanetary magnetic field By : A conceptual model and simulations, *J.*
564 *Geophys. Res.*, *101(A3)*, 4907–4916, doi:10.1029/95JA03673.
565 Kim, H.-J., and A. A. Chan (1997), Fully adiabatic changes in storm-time relativistic
566 electron fluxes, *J. Geophys. Res.*, *102(A10)*, 22,107, doi:10.1029/97JA01814.

Kim, K. C., D.-Y. Lee, H.-J. Kim, L. R. Lyons, E. S. Lee, M. K. Öztürk, and C. R. Choi (2008), Numerical calculations of relativistic electron drift loss effect, *J. Geophys. Res.*, *113*, A09212, doi:10.1029/2007JA013011.

Kletzing, C. A., et al. (2013), The Electric and Magnetic Field Instrument Suite and Integrated Science (EMFISIS) on RBSP, *Space Sci. Rev.*, *179*, 127–181, doi:10.1007/S11214-013-9993-6.

Kozyra, J. U., V. K. Jordanova, R. B. Horne, and R. M. Thorne (1997), Modeling of the contribution of electromagnetic ion cyclotron (EMIC) waves to stormtime ring current erosion, in magnetic storms, *American Geophysical Union, Washington, D. C.*, *Geophys. Monogr. Ser., Vol. 98, edited by B. T. Tsurutani et al.*, 187–202, doi: 10.1029/GM098p0187.

Lee, J., J. Hwang, E. Lee, Y. Kim, Y. Park, G. K. Parks, and D. G. Sibeck (2013), Observation of plasma depletions in outer radiation belt by van allen probes, *Eos Trans. AGU*, pp. SM33A–2165.

Li, X., et al. (1997), Multi-satellite observations of the outer zone electron variation during the Nov. 3-4 1993 magnetic storm, *J. Geophys. Res.*, *102(A7)*, 14,123, doi: 10.1029/97JA01101.

Loto'aniu, T. M., I. R. Mann, L. G. Ozeke, A. A. Chan, Z. C. Dent, and D. K. Milling (2006), Radial diffusion of relativistic electrons into the radiation belt slot region during the 2003 Halloween geomagnetic storms, *J. Geophys. Res.*, *111*, A04218, doi: 10.1029/2005JA011355.

Loto'aniu, T. M., H. J. Singer, C. L. Waters, V. Angelopoulos, I. R. Mann, S. R. Elkington, and J. W. Bonnell (2010), Relativistic electron loss due to ultralow frequency

waves and enhanced outward radial diffusion, *J. Geophys. Res.*, *115*, A12245, doi: 10.1029/2010JA015755.

Lundquist, S. (1950), Magnetohydrostatic fields, *Ark. Fys.*, *2*, 361.

MacDonald, E., et al. (2013), Low energy plasma measurements of the Van Allen Probes crossing open field lines, *Eos Trans. AGU*, pp. SM43A–02.

Mauk, B. H., N. J. Fox, S. G. Kanekal, R. L. Kessel, D. G. Sibeck, and A. Ukhorskiy (2013), Science objectives and rationale for the Radiation Belt Storm Probes Mission, *Space Sci. Rev.*, *179*, 3–27, doi:10.1007/s11214-012-9908-y.

McFadden, J. P., C. W. Carlson, D. Larson, M. Ludlam, R. Abiad, B. Elliott, P. Turin, M. Marckwordt, and V. Angelopoulos (2008), The THEMIS ESA plasma instrument and in-flight calibration, *Space Sci. Rev.*, *141*, 277–302, doi:10.1007/s11214-008-9440-2.

McIlwain, C. E. (1966), Ring current effects on trapped particles, *J. Geophys. Res.*, *71*, 3623, doi:10.1029/JZ071i015p03623.

Mende, S. B., S. E. Harris, H. U. Frey, V. Angelopoulos, C. T. Russell, E. Donovan, B. Jackel, M. Greffen, and L. M. Peticolas (2008), The themis array of ground-based observatories for the study of auroral substorms, *Space Sci. Rev.*, *141*, 357, doi: 10.1007/s11214-11008-19380-x.

Meredith, N., R. B. Horne, and R. R. Anderson (2001), Substorm dependence of chorus amplitudes: implications for the acceleration of electrons to relativistic energies, *J. Geophys. Res.*, *106*, 13,165, doi:10.1029/2000JA900156.

Meredith, N., M. Cain, R. B. Horne, R. M. Thorne, D. Summers, and R. R. Anderson (2003), Evidence for chorus-driven electron acceleration to relativistic energies from a survey of geomagnetically disturbed periods, *J. Geophys. Res.*, *108*, A61248, doi:

613 10.1029/2002JA009764.

614 Meredith, N., R. B. Horne, M. A. Cliverd, D. Horsfall, R. R. M. Thorne, and R. R.
615 Anderson (2006), Origins of plasmasheric hiss, *J. Geophys. Res.*, *111*, A09217, doi:
616 10.1029/2006JA011707.

617 Millan, R., and R. M. Thorne (2007), Review of radiation belt relativistic electron losses,
618 *J. Atmos. Solar Terr. Phys.*, *69*, 362, doi:10.1016/j.jastp.2006.06.019.

619 Nishimura, Y., A. Shinbori, T. Ono, M. Iizima, and A. Kumamoto (2007), Evolution of
620 ring current and radiation belt particles under the influence of storm-time electric fields,
621 *J. Geophys. Res.*, *112*, A06241, doi:10.1029/2006JA012177.

622 O'Brien, T. P., K. R. McPherron, I. R. Mann, N. P. Meredith, J. B. Blake, J. F. Fennell,
623 M. D. Looper, D. K. Milling, and R. R. Anderson (2003), Energization of relativistic
624 electron in the response of ULF power and MeV microbursts: Evidence for dual ULF
625 and VLF acceleration, *J. Geophys. Res.*, *108(A08)*, 1329, doi:10.1029/2002JA009784.

626 Onsager, T., R. Grubb, J. Kunches, L. Matheson, D. Speich, R. Zwickl, and H. Sauer
627 (1996), Operational uses of the GOES energetic particle detectors, *Proc. SPIE 2812,*
628 *GOES-8 and Beyond*, p. 281, doi:10.1117/12.254075.

629 Onsager, T. G., G. Rostoker, H.-J. Kim, G. D. Reeves, T. Obara, H. J. Singer,
630 and C. Smithtro (2002), Radiation belt electron flux dropouts: Local time, ra-
631 dial, and particle-energy dependence, *J. Geophys. Res.*, *107(A11)*, 1382, doi:
632 10.1029/2001ja000187.

633 Paschmann, G., A. N. Fazakerley, and S. Schwartz (1998), Moments of plasma velocity
634 distributions, in *Analysis methods for multi-spacecraft data*, edited by G. Paschmann
635 and P. W. Daly, p. 125, ESA Publications Division, Keplerlaan 1, 2200 AG Noordwijk,

636 The Netherlands.

637 Reeves, G. D., R. D. Belian, T. C. Cayton, M. G. Henderson, R. A. Christensen, M. P. S,
638 and J. C. Ingraham (1997), Using Los Alamos geosynchronous energetic particle data
639 in support of other missions, *In: Lockwood, M., Opgenoorth, H.J., Wild, M.N., Stampe,*
640 *R. (Eds.), Satellite-Ground Based Coordination Source book*, pp. 263–272.

641 Reeves, G. D., et al. (2013), Electron acceleration in the heart of the Van Allen radiation
642 belts, *Science*, *341(6419)*, 991–994, doi:10.1126/science.1237743.

643 Rostoker, G., S. Skone, and D. N. Baker (1998), On the origin of relativistic electrons
644 in the magnetosphere associated with some geomagnetic storms, *Geophys. Res. Lett.*,
645 *25(19)*, 3701, doi:10.1029/ 98GL02801.

646 Sangalli, L., N. Partamies, M. Syrjösuo, C.-F. Enell, K. Kauristie, and S. Mäkinen
647 (2011), Performance study of the new EMCCD-based all-sky cameras for au-
648 roral imaging, *International Journal of Remote Sensing*, *32:11*, 2987–3003, doi:
649 10.1080/01431161.2010.541505.

650 Shirataka, N., M. Fujimoto, H. Hasegawa, and R. TanDokoro (2006), Reproducing the
651 bipolar magnetic signature at the jet leading edge by three-dimensional reconnection
652 with nonzero guide field, *J. Geophys. Res.*, *111*, A07201, doi:10.1029/2005JA011521.

653 Shprits, Y., M. Daae, and B. Ni (2012), Statistical analysis of phase space density buildups
654 and dropouts, *J. Geophys. Res.*, *117*, A01219, doi:10.1029/2011JA016939.

655 Shprits, Y. Y., R. M. Thorne, R. Friedel, G. D. Reeves, J. F. Fennell, D. Baker, and S. G.
656 Kanekal (2006), Outward radial diffusion driven by losses at magnetopause, *J. Geophys.*
657 *Res.*, *111*, A11214, doi:10.1029/2006JA011657.

Singer, H., L. Matheson, R. Grubb, A. Newman, and D. Bouwer (1996), Monitoring space weather with the GOES magnetometers, *Proc. SPIE 2812, GOES-8 and Beyond*, p. 299, doi:10.1117/12.254077.

Spence, H. E., et al. (2013), Science goals and overview of the Radiation Belt Storm Probes (RBSP) Energetic Particle, Composition, and Thermal Plasma (ECT) Suite on NASA's Van Allen Probes Mission, *Space Sci. Rev.*, *179*, 311–336, doi:10.1007/s11214-013-0007-5.

Summers, D., and R. M. Thorne (2003), Relativistic electron pitch angle scattering by electromagnetic ion cyclotron waves during geomagnetic storms, *J. Geophys. Res.*, *108(A04)*, 1143, doi:10.1029/2002JA009489.

Thorne, R. M. (2010), Radiation belt dynamics: The importance of wave-particle interactions, *Geophys. Res. Lett.*, *37*, L22107, doi:10.1029/2010GL044990.

Thorne, R. M., T. P. O'Brien, Y. Y. Shprits, D. Summers, and R. B. Horne (2005), Timescale for MeV electron microburst loss during geomagnetic storms, *J. Geophys. Res.*, *110*, A09202, doi:10.1029/2004JA010882.

Thorne, R. M., et al. (2013), Rapid local acceleration of relativistic radiation-belt electrons by magnetospheric chorus, *Nature*, *504*, 411–414, doi:10.1038/nature12889.

Tsyganenko, N. A. (1995), Modeling the Earth's magnetospheric magnetic field confined within a realistic magnetopause, *J. Geophys. Res.*, *100*, 5599.

Turner, D. L., Y. Shprits, M. Hartinger, and V. Angelopoulos (2012), Explaining sudden losses of outer radiation belt electrons during geomagnetic storms, *Nature Phys.*, *8*, 208, doi:10.1038/nphys2185.

680 Ukhorskiy, A. Y., and M. I. Sitnov (2008), Radial transport in the outer radiation belt
681 due to global magnetospheric compressions, *J. Atmos. Sol. Terr. Phys.*, *70*, 1714, doi:
682 10.1029/2007JA013011.

	RBSP-B	RBSP-A	Geotail	LANL-97A	LANL-04A	LANL-02A	1994-084	GOES-13	GOES-14	GOES-15	1991-080
							0111 0112	0115 0117	0128:30 0131		0127, 0144
1st dropout	0157 0200	0200 0202	0202:30 0204	0159:50 0202	0203 0209	0211 0215	0155 0157:30			0200 0202	0206 0208
2nd dropout	0245 0247	0246 0249:50	0301 0303				0226, 0236 (weak)			0230 0232	0319-0338
3rd dropout	0334 0338	0335:30 0340		0336 0337:30	0355:30 0359	0403 0406	0306 0309		0316 0318	0325 0327	0355-0421
4th dropout	0415 0417:30	0420 0422	0415:15 0416:15				0357 0359:30	0400:30 0405	0402:30 0406	0403:20 0406:30	
5th dropout	0442:30 0445	0441 0445		0445 0446	0455 0457	0500 0503	0417			0428 0430:15	0433-0509
6th dropout	0506:30 0508						0513 0529			0521:20 0524	

Table 1. Observation times for Van Allen Probes, GOES, LANL, and Geotail spacecraft detection of the onset tie (upper times in UT) and the peak flux depression time (lower times) of the series of flux reduction. Extended dropout timings, 0205–0301 UT, 0305–0338 UT, 0353–0422 UT, and 0433–0509 UT are shown for LANL 1991-080. Times of weak flux reductions are parenthesized. A thick vertical line separates the dawnside (left-hand side) and the duskside (right-hand side) observations.

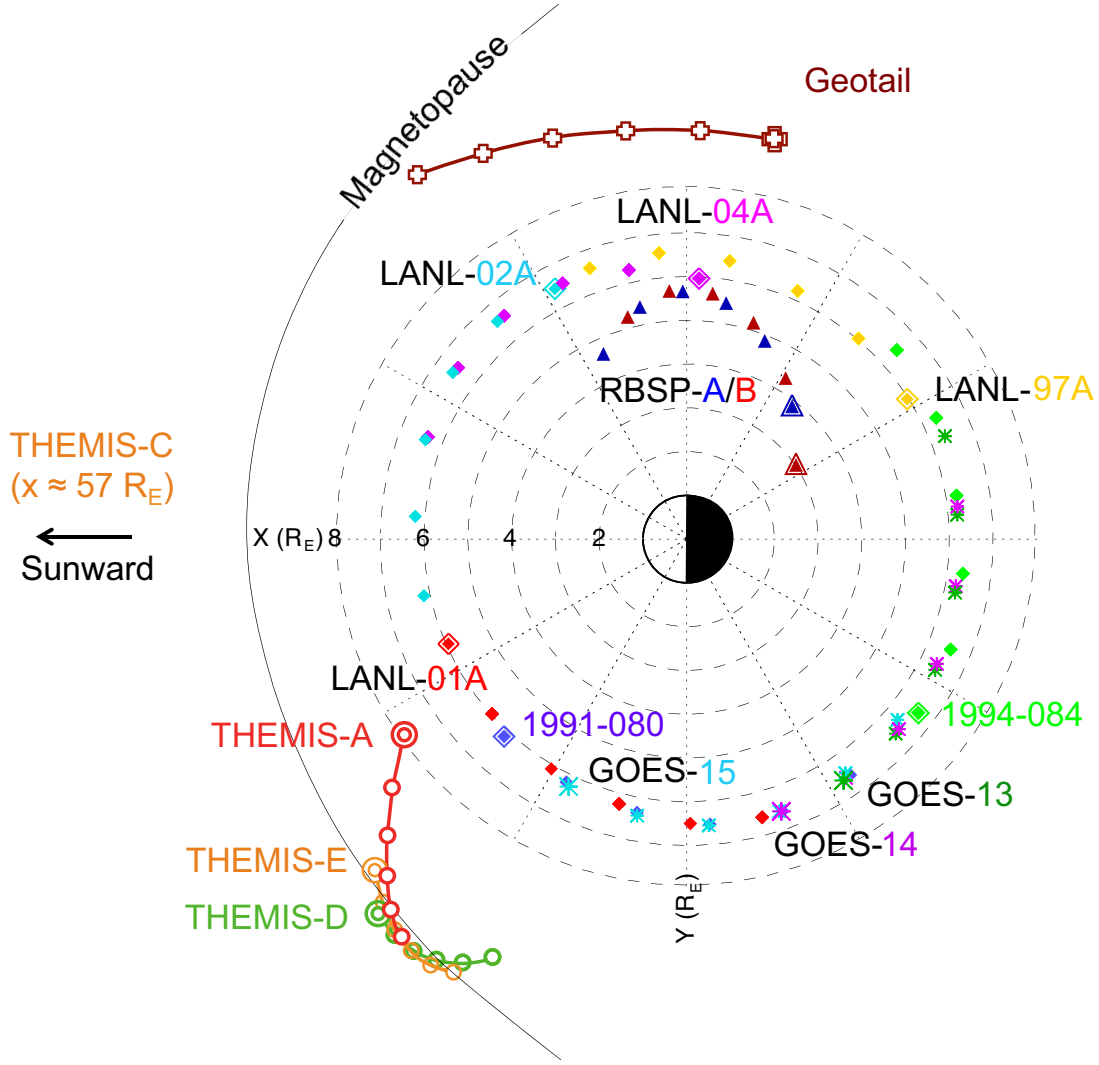

Figure 1. Location of Van Allen Probes (RBSP), GOES, LANL, Geotail, and THEMIS during 0100-0600 UT on 14 Nov, 2012 in the GSM XY plane. Each of six marks corresponds to the spacecraft location at 1–large mark to 6 UT by an hourly cadense. Two ARTEMIS probes in the upstream solar wind at $x \approx 57$ R_E are indicated.

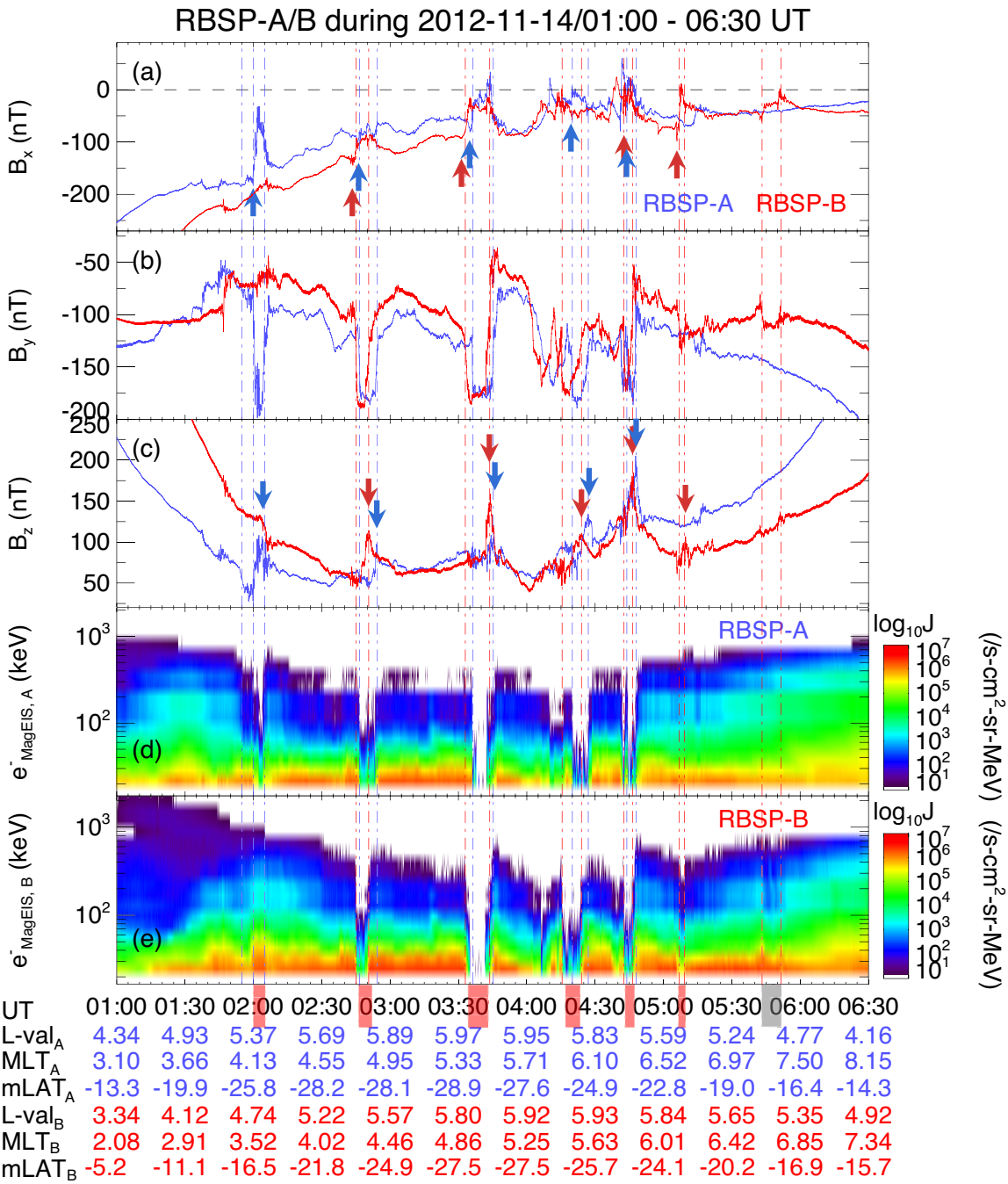

Figure 2. Van Allen Probes observations of a series of particle flux dropouts: (a-c) the (x, y, z) components of the magnetic field measured by RBSP-A (blue) and RBSP-B (red), (d, e) the electron flux spectrogram measured by the ECT/MagEIS instrument aboard RBSP-A (d) and RBSP-B (e). The magnetic latitudes shown in the bottom ephemeris are obtained from the T96 model [*Tsyganenko*, 1995].

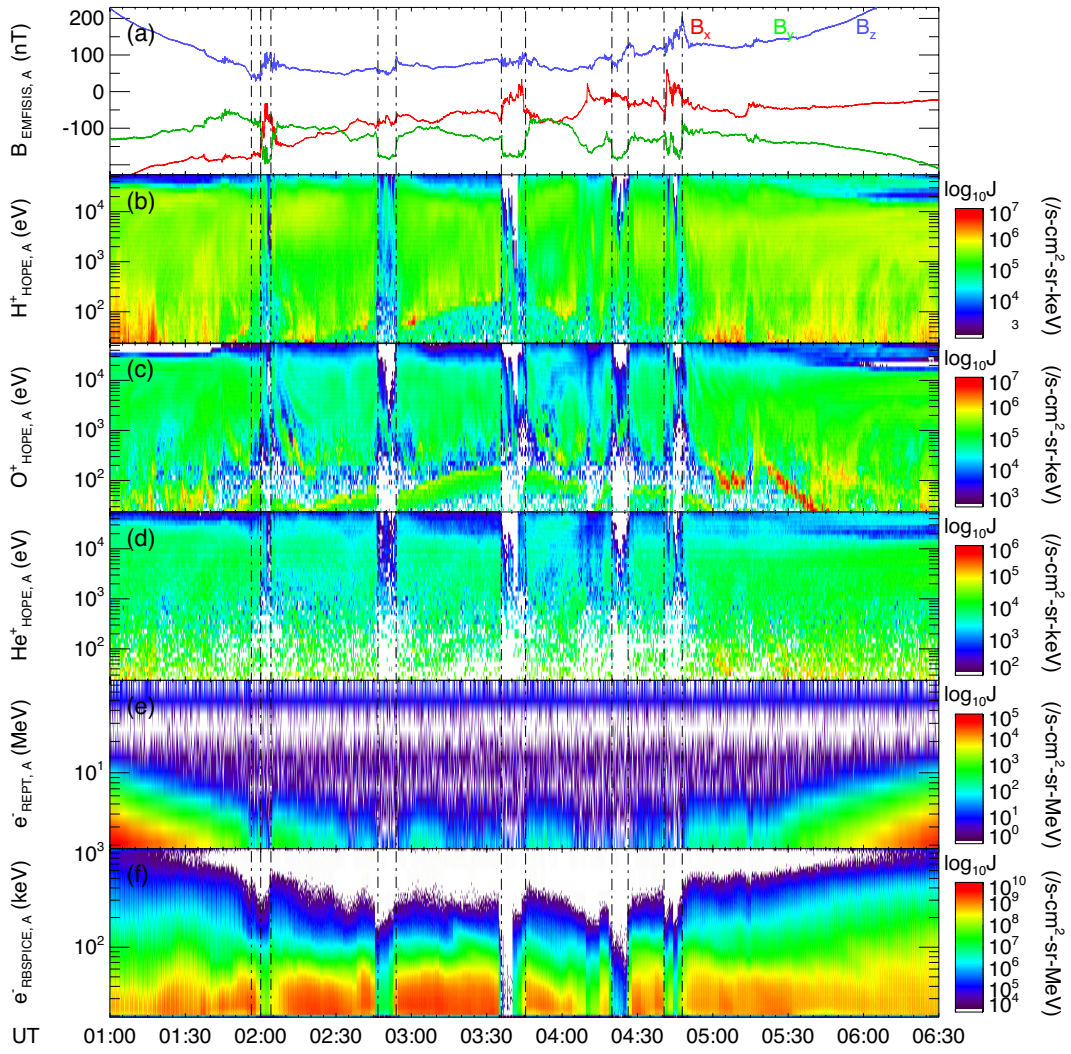

Figure 3. Van Allen Probes (RBSP)-A observations of the dropouts seen for multi-species ions and both thermal and energetic electrons measured by ECT/HOPE (b-d), ECT/REPT (e), and RBSPICE (d). The corresponding magnetic field changes are shown in the top panel (a). Note that the enhanced low-energy ions observed by HOPE are due to the effects of spacecraft potential, which is elevated during the storm time and accelerates these low-energy particles into the detector.

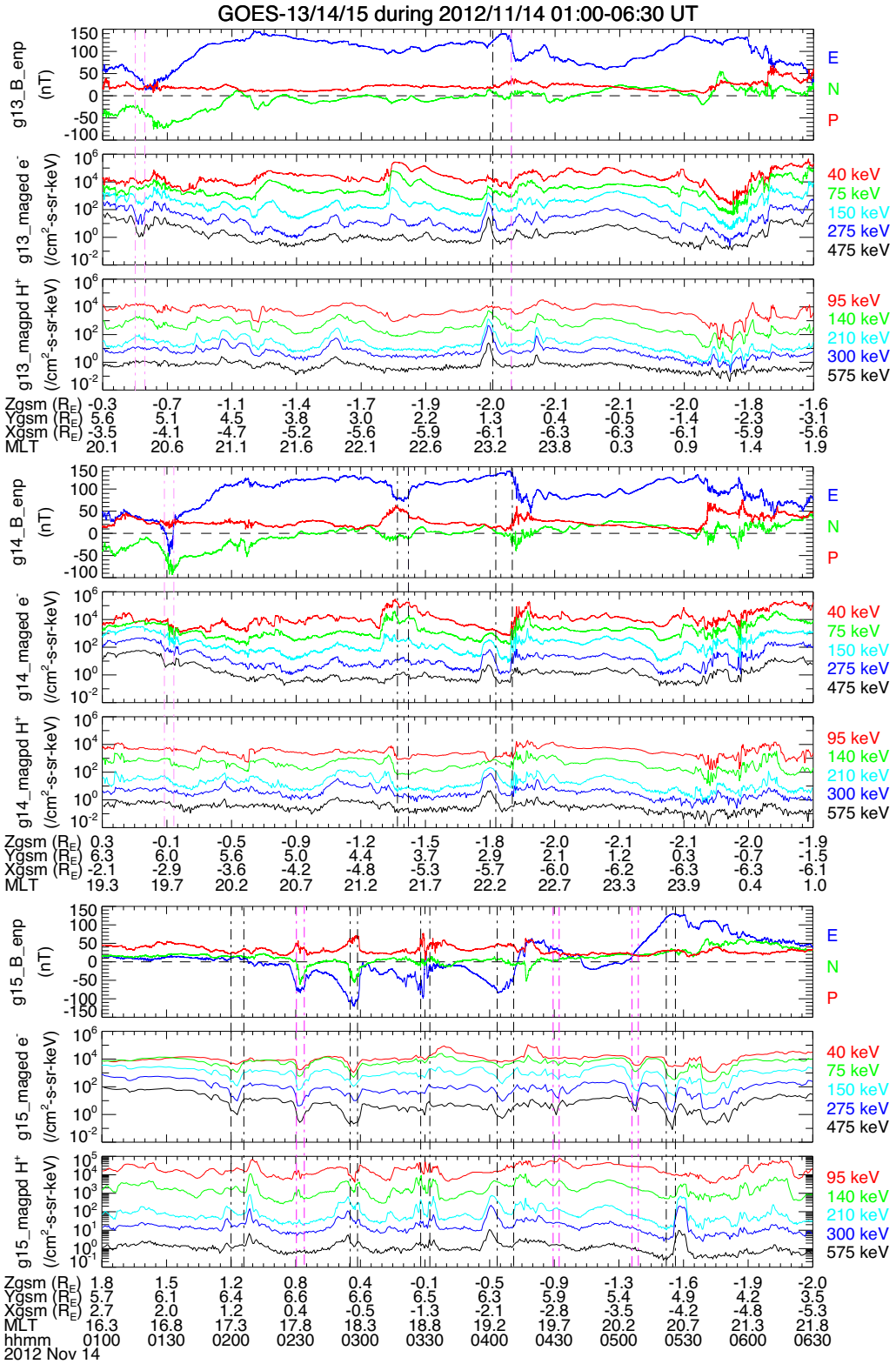

Figure 4. Three GOES spacecraft, GOES-13, 14, and 15 observations of the magnetic field with E (earthward), N (eastward) and P (northward) components and particle fluxes of electrons and protons during 0100–0630 UT.

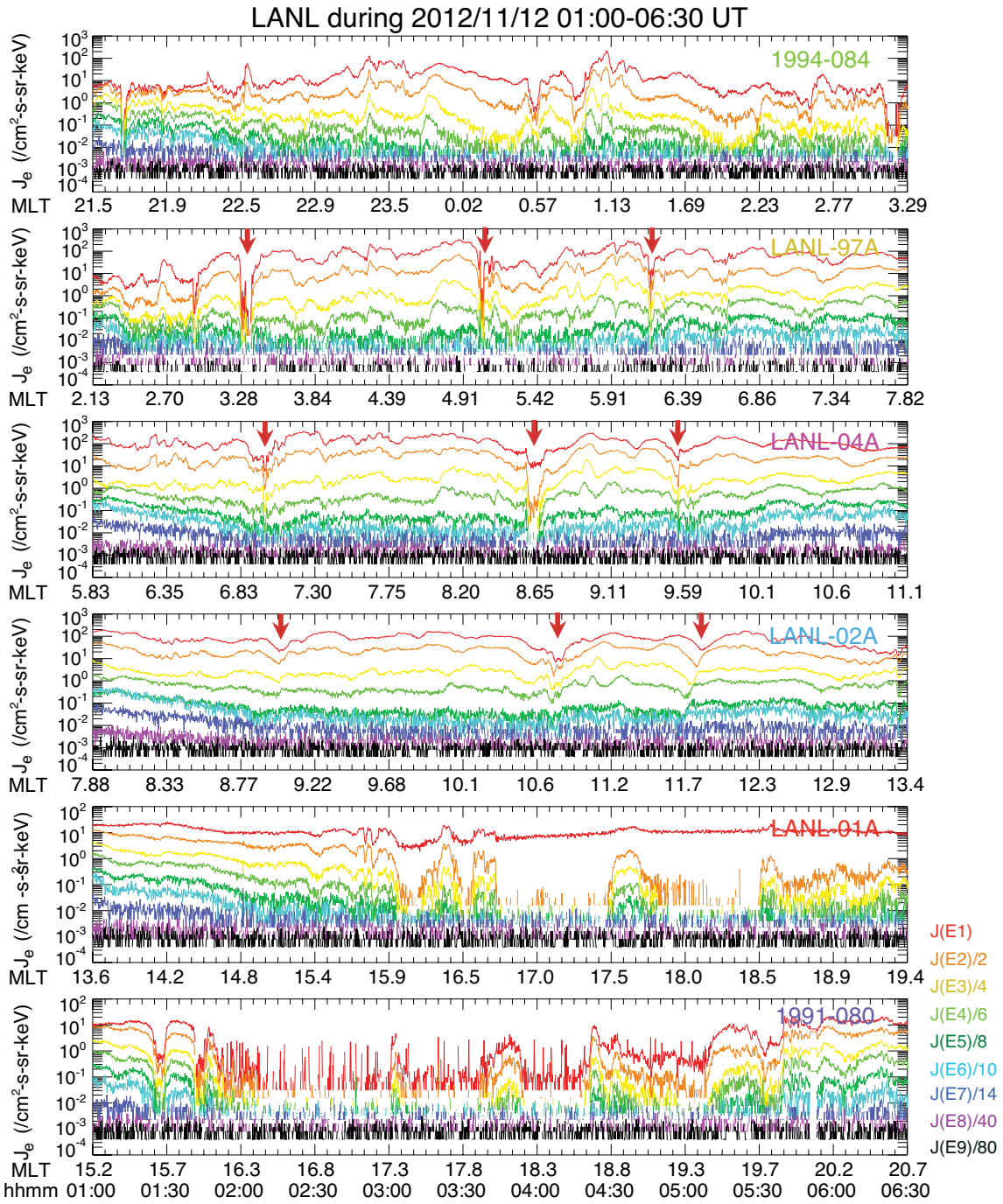

Figure 5. LANL spacecraft observations of dropouts in electron flux. Colored profiles represent electron flux in nine (E1 to E9) differential energy channels (E1: 50–75 keV, E2: 75–105 keV, E3: 105–150 keV, E4: 150–225 keV, E5: 225–315 keV, E6: 315–500 keV, E7: 500–750 keV, E8: 750–1100 keV, and E9: 1100–1500 keV). Weighting is applied for a better viewing of the flux variations.

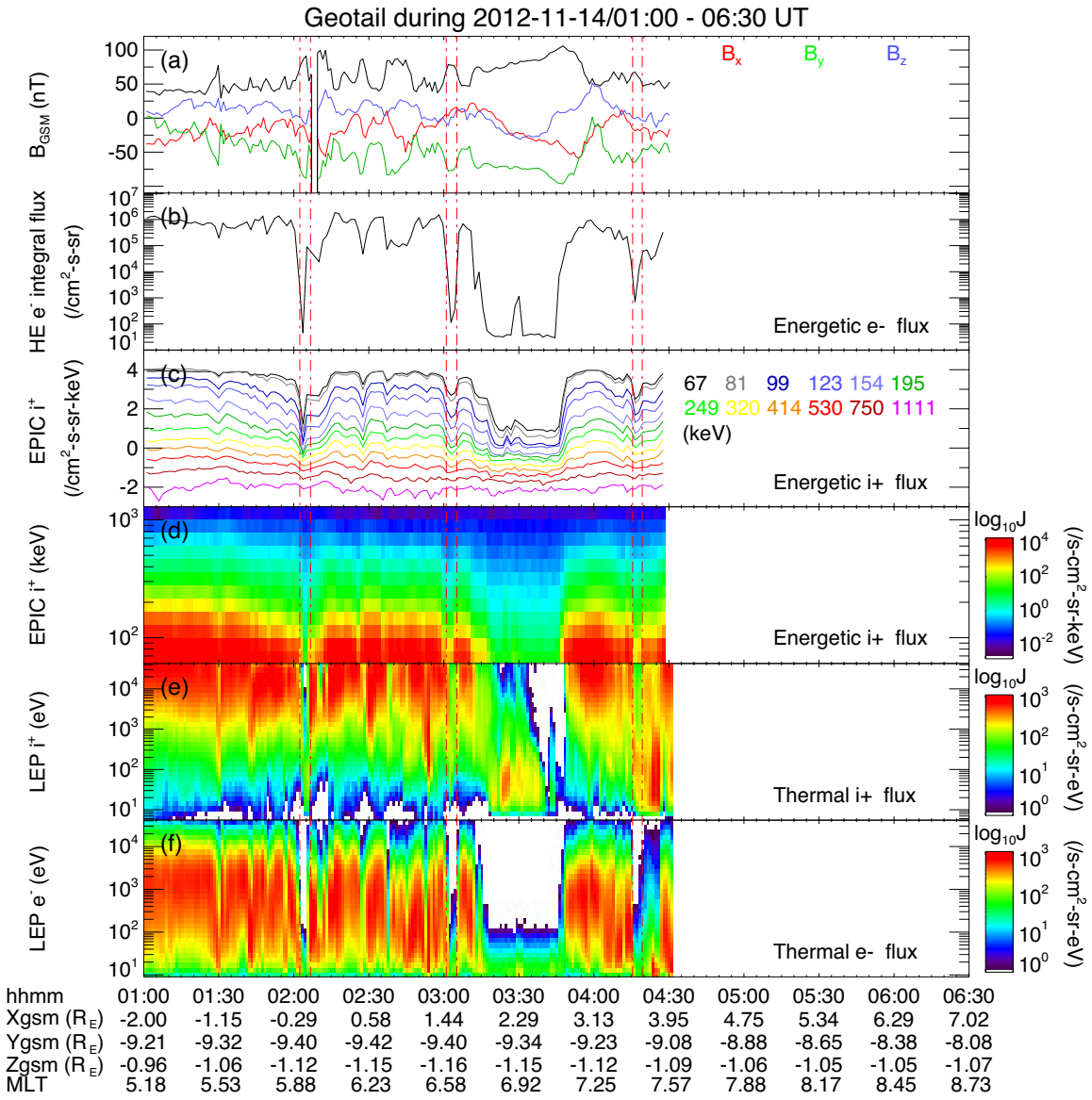

Figure 6. Geotail spacecraft observations: (a) magnetic field, (b) energetic electron flux, (c, d) energetic ion flux, (e, f) thermal ion and electron flux. Note a data gap between 0430 UT and 0630 UT.

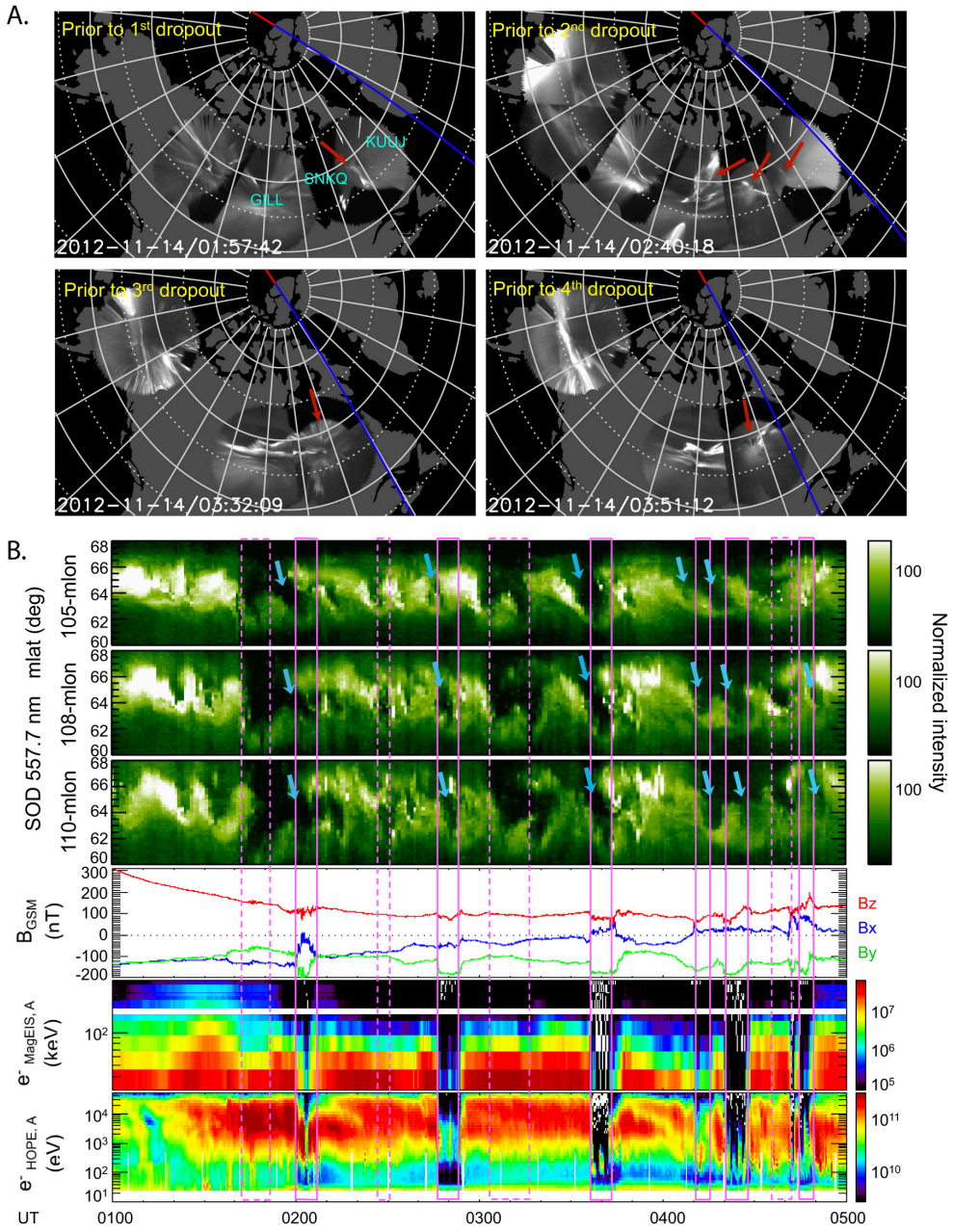

Figure 7. A. THEMIS All-Sky Imager (ASI) data showing narrow north-south auroral forms, called auroral streamers, prior to the first to the fourth dropout. Blue line denotes the midnight meridian. B. Auroral keogram at multiple magnetic longitudes recorded from the Sodankylä station (SOD) in Finland close to magnetic footprints of the Van Allen Probes. Disappearance of auroral intensifications that are possibly Omega bands are correlated with the Van Allen Probes observations of flux dropouts, indicated by vertical solid lines. Vertical dashed lines mark no clear correlations.

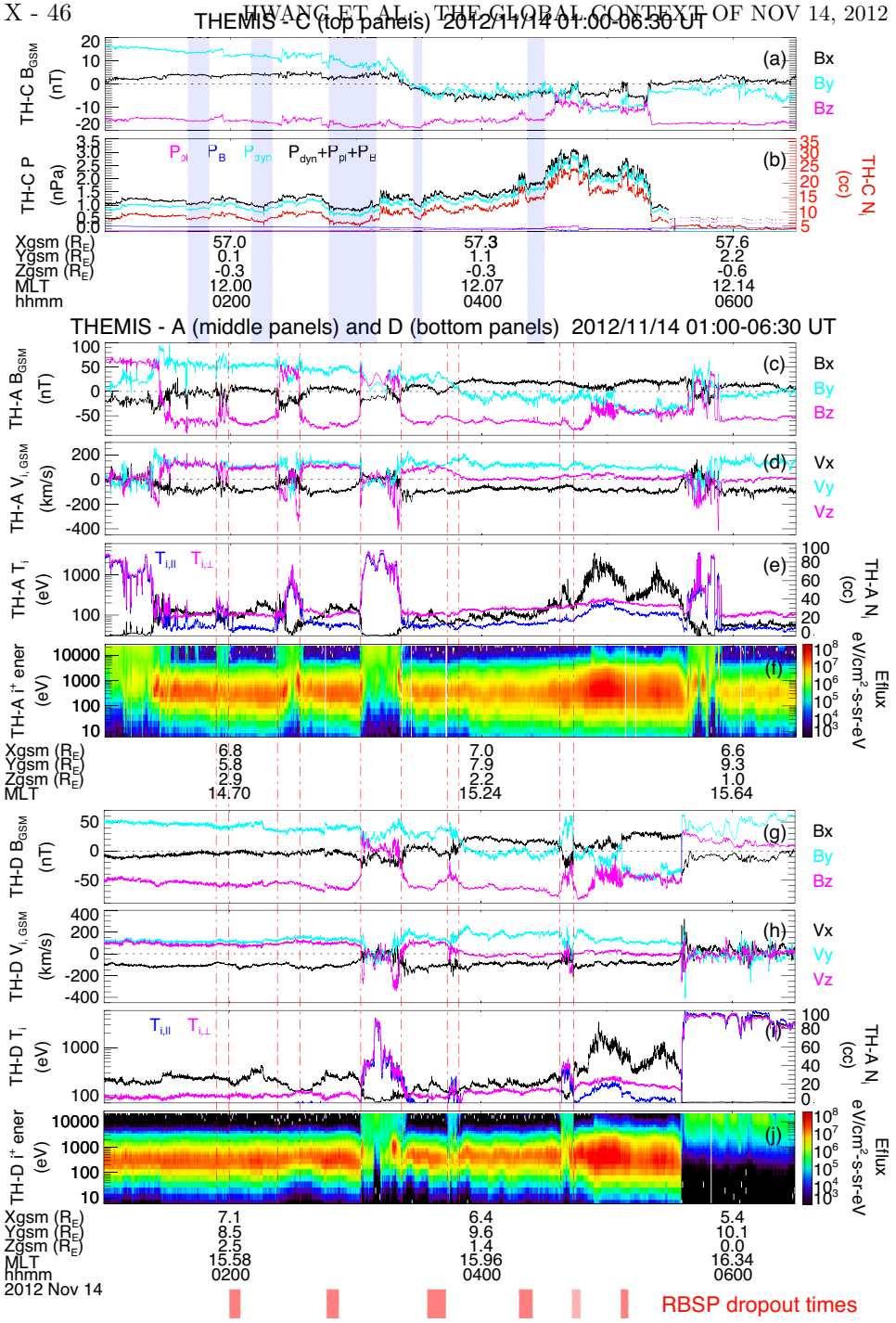

Figure 8. Observations by ARTEMIS (THEMIS-C) spacecraft, lying mostly on the Sun-Earth line ($x =\sim 57$ R_E) and THEMIS-A and D passing the postnoon-side magnetopause during the event: (a) the IMF and (b) the solar wind pressure and density observed by THEMIS-C (top panels), (c, g) the magnetic field, (d, h) the flow velocity of bulk plasmas, (e, i) the plasma temperature and density, and (f, j) the ion energy spectrogram measured by THEMIS-A (middle panels) and D (bottom panels).

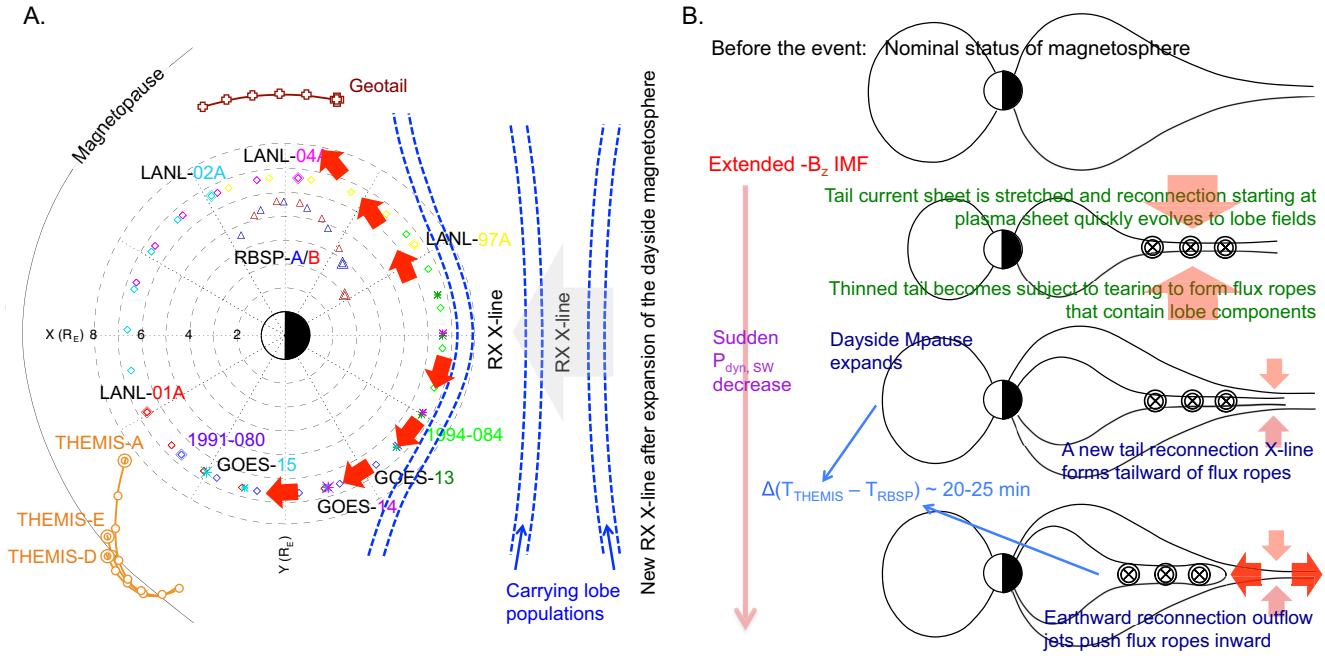

Figure 9. Illustrations of the flux-rope hypothesis where the flux-depleted regions are interpreted as magnetic flux bundles or flux ropes, shown in the equatorial (xy) plane (A) and meridional (xz) picture in sequence (B): During the extended strong southward IMF, the tail current sheet is highly stretched, compard to a nominal status (top cartoon, B), that reconnection starting at plasma sheet involves lobe fields with time. The thinned current sheet also becomes subject to tearing instability to form magnetic flux ropes that contain lobe components as a result of lobe reconnection. Under sudden intermittent period of the solar wind dynamic pressure decrease (or other unknown causes inherent in the solar wind), the dayside magnetopause expands and a new tail reconnection X-line forms tailward of the previously-formed flux ropes. Earthward reconnection jets push those flux ropes inward. They cannot penetrate all the way into the inner magnetosphere due to pressure boundary, where they start to wrap and move around the boundary (A).

A.

	RBSP-A: boundary normal	RBSP-A: $\frac{\lambda_{mid}}{\lambda_{min}}$	RBSP-B: boundary normal	RBSP-B: $\frac{\lambda_{mid}}{\lambda_{min}}$
1st dropout inbound	-0.378, 0.023, 0.926	2.20		
1st dropout outbound	0.608, 0.545, -0.577	5.73		
2nd dropout inbound	0.166, -0.216, 0.962	9.37	0.185, 0.039, 0.982	6.35
2nd dropout outbound	0.928, -0.313, -0.199	10.6	0.990, 0.030, -0.137	10.1
3rd dropout inbound	-0.330, -0.369, 0.869	2.67	-0.066, 0.043, 0.997	2.96
3rd dropout outbound	0.301, 0.365, 0.881	4.59	0.878, 0.203, -0.433	15.9
4th dropout inbound	0.132, 0.297, 0.946	7.59	-0.083, 0.147, 0.986	3.15
4th dropout outbound	0.946, 0.273, 0.175	6.66	0.941, -0.321, -0.105	5.80
5th dropout inbound	0.352, 0.855, 0.380	4.73	0.370, 0.730, -0.575	7.85
5th dropout outbound	0.901, 0.433, 0.011	9.97	0.880, 0.297, -0.372	9.05
6th dropout inbound			-0.253, -0.538, 0.804	2.24
6th dropout outbound			0.743, 0.664, -0.080	4.18

B.

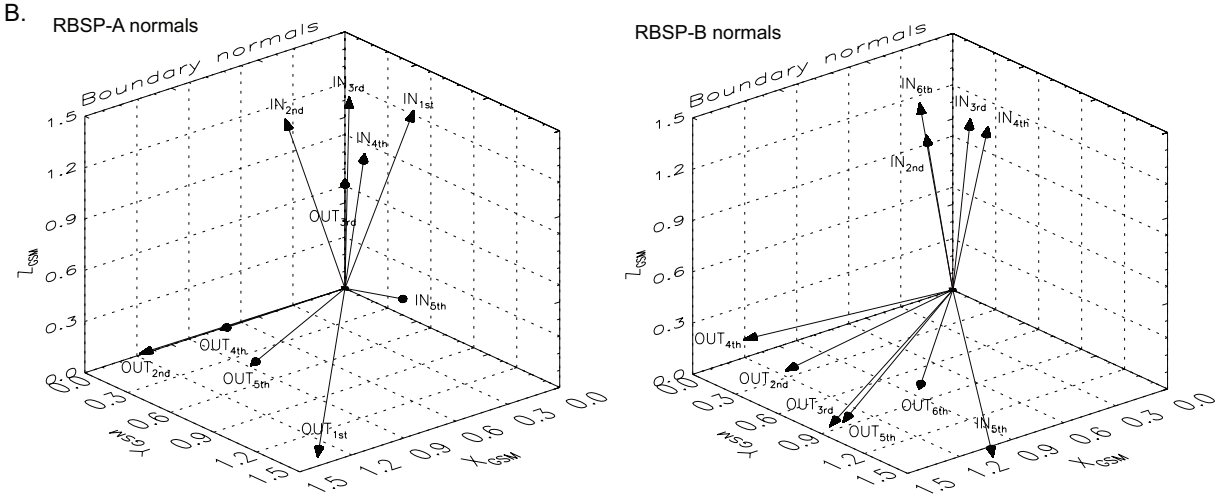

Figure 10. A. Boundary normals in GSM coordinates during the inbound and outbound crossings of each dropout region by the Van Allen Probes, calculated from the magnetic-field minimum variance analysis. The medium-to-minimum eigenvalue ratio in the minimum variance calculation is shown. The bootstrap error estimate for the minimum variance analysis [*Kawano and Higuchi*, 1995] shows a standard deviation of $\leq$0.047. B. Illustrations of boundary normals observed at RBSP-A (left) and RBSP-B (right). For a majority of those boundaries, the inbound (outbound) normal when the Van Allen Probes entering (exiting) the flux dropout region mainly points along the z (x) direction.

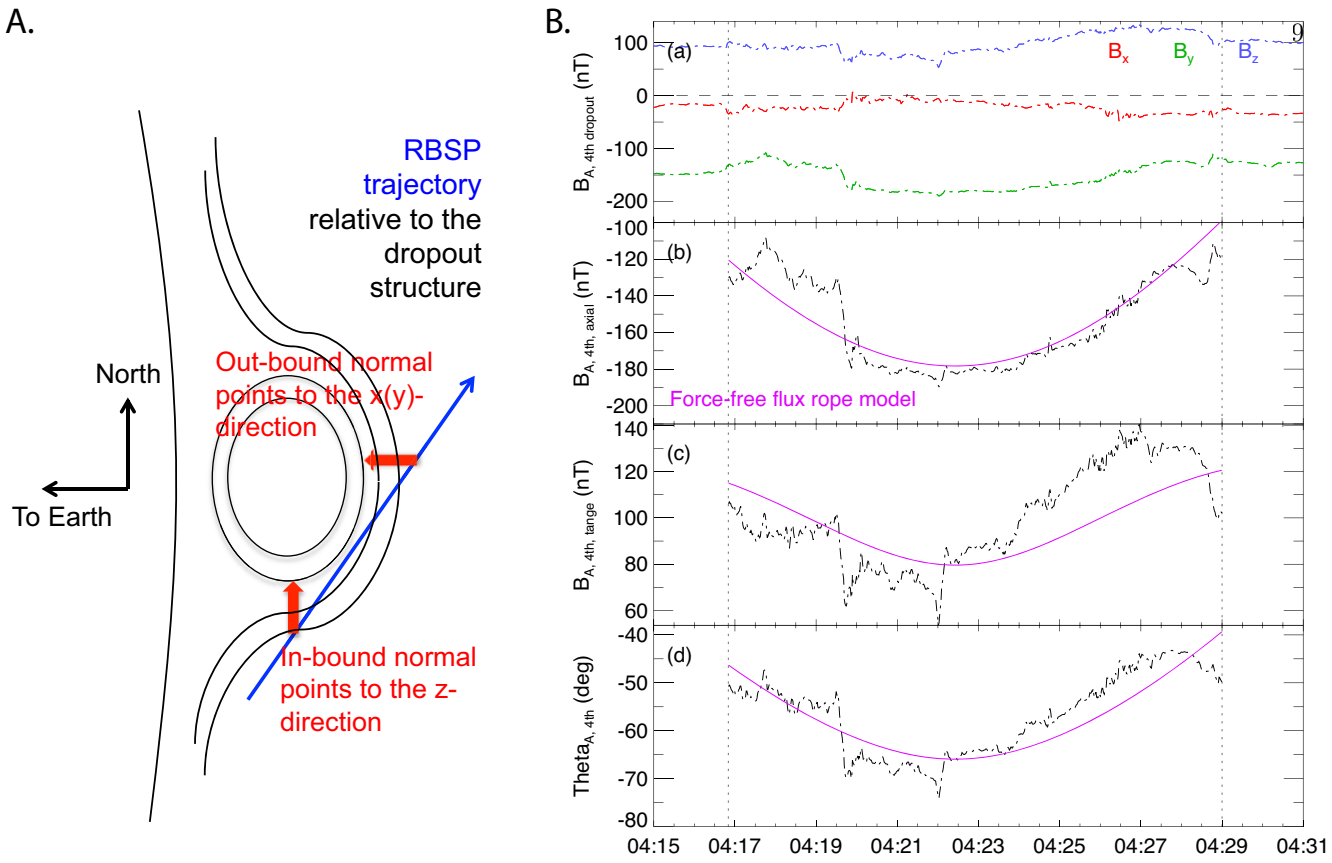

Figure 11. A. Illustration of the relative trajectory of the Van Allen Probes in the frame of the magnetic flux rope. This cartoon well explains a little dip (increase in magnitude) in B_x components and sharp increases in B_z components at the entrance and exit of each dropout, respectively, as shown in Figure 2(a and c). B. Fitting the observed magnetic field profiles (a) during a single period (the fourth flux dropout at ∼0417–0429 UT) among the sequential flux-dropout structures to a force-free flux rope model, where $\mu_0\mathbf{J} = \alpha\mathbf{B}$ (so that $\mathbf{J} \times \mathbf{B} = 0$). The flux rope in a force-free configuration has cylindrical symmetry, represented by the axial (B_A), tangential (B_T), and radial (B_R) components of the magnetic field. Axial (b) and tangential (c) components, and the angle (d) made by the axial component to the total magnetic strength (with 90° corresponding to the core of the flux rope) are shown in dot-dashed curves. Overplotted are the model values shown in solid curves.